On the Transfer of Momentum by Trapped Lee Waves: Case of the IOP 3 of PYREX

MARC GEORGELIN

Laboratoire d'Aérologie, Université Paul Sabatier, Toulouse, France

FRANÇOIS LOTT

Laboratoire de Météorologie Dynamique du CNRS, Université Pierre et Marie Curie, Paris, France

ABSTRACT

The airplane data collected between 4 and 12 km above the Pyrénées during the intensive observation period (IOP) 3 of the Pyrénées Experiment (PYREX) are analyzed again. A spectral analysis of the velocity and potential temperature series shows that the mountain waves are dominated by two oscillations with well-defined horizontal wavenumbers. At nearly all altitudes, at least one among these two oscillations can be extracted: the short oscillation dominates the signal below 6 km and the long one above. These two oscillations contribute to the Reynolds stress below 5 km and not above.

Linear steady nondissipative simulations show that the short oscillation is a trapped resonant mode and the long one a leaking, or partially leaking, resonant mode of the background flow. Pseudo-momentum flux budgets show that the short resonant mode only contributes to the Reynolds stress at low level (here below 3 to 4 km typically) while the long one contributes to the Reynolds stress at all levels. At low level, (below 4 to 6 km typically), the long mode can induce a decay of the Reynolds stress amplitude, when it partially leaks toward the stratosphere. Various tests, changing the incident flow profiles within limits provided by the different soundings available this day, reveal, on the one hand, that the above findings are quite robust. On the other hand, they reveal that the resonant modes response is very sensitive to the background flow and orography specifications.

In some of the steady linear simulations, the long resonant oscillation has a Reynolds stress that is constant with altitude. In all of them the downwind extent of the lee waves is overestimated and the waves amplitude is too large. To explain these mismatches with the observations, we present simulations that last 3 h only, so the resonant modes patterns are everywhere unsteady. They show that during their build-up phase, all the leaking modes can make the Reynolds stress amplitude decays with altitude at low level (here below 4 to 6 km, typically). At this time, the downstream extent of the waves is also correctly predicted. These linear unsteady simulations also give realistic waves amplitude and Reynolds stress profiles if the mountain is cut off to parameterize nonlinear low-level flow splitting.

By using a nonlinear model, the simulated waves are matched to that observed through an adjustment of the parameters of the turbulent diffusion parameterization scheme: with enough dissipation, the model response can become quite realistic. In these nonlinear simulations, the background flow is chosen so that there is only one resonant mode and this mode does not contribute much to the Reynolds stress in the inviscid case. When increasing the mountain height and the dissipation, the overall structure of that mode stays unchanged, and it never contributes much to the Reynolds stress. This indicates that the dissipative and nonlinear processes alone are not likely to produce the observed low-level stress variations associated with the resonant modes.

1. Introduction

During the past three decades, considerable researches have been done on the dynamics of atmospheric flow around and over mountains with scales varying between a few kilometers and a few hundred kilometers. They follow early studies by Queney (1947) and Scorer (1949), which show that mountains can generate gravity waves that transfer momentum from the ground to the

atmosphere (Eliassen and Palm 1961). Following these studies, more recent works focused on the nonlinear aspect of 2D mountain flow (Long 1953; Smith 1985; Durran 1986; Laprise and Peltier 1989) to explain lee-ward foehns and downslope windstorms. Others focused on the structure of 3D mountain waves (Phillips 1984), on the dynamics of nonlinear 3D mountain flow (Miranda and James 1992; Schär and Smith 1993; Schär and Durran 1997) and on the related low-level flow splitting.

Among the different practical motivations for these studies, one concern is the parameterization of mountain gravity wave drag in weather forecasting and climate models (Boer et al. 1984; Palmer et al. 1986). In most

Corresponding author address: François Lott, Laboratoire de Météorologie Dynamique du CNRS, UPMC Paris 6, case 99, 4 Place Jussieu, 75252 Paris Cedex 05, France.
E-mail: flott@lmd.jussieu.fr

parameterization schemes, it is assumed that the wave Reynolds stress is constant with altitude when the background mean wind $U(z)$ has a constant sign, and in the absence of breaking (Eliassen and Palm 1961). Nevertheless, it is now well established that this kind of parameterization is only half supported by observations. The mountain gravity wave drag predicts well the drag measured at ground level (Bessemoulin et al. 1993) but overstates, by nearly an order of magnitude, the Reynolds stress measured by airplanes aloft. In the mesoscale context (i.e., neglecting the Coriolis force), this discrepancy between the measured mountain drag and the measured stresses has essentially five origins:

1) the wave dissipation in the boundary layer (Georgelin et al. 1994) or the breaking of the waves at low level (Miranda and James 1992);
2) the unsteady nature of the waves due to the time variations of the incident flow (Bell 1975; Lott and Teitelbaum 1993);
3) the downstream transfer of momentum by trapped waves (Bretherton 1969; Durran 1995; Lott 1998), or simply the fact that the Reynolds stress is measured over a finite distance so even nontrapped waves can induce nonzero momentum fluxes through the domain downwind lateral boundary (Keller 1994);
4) the momentum flux leakage that occurs through the domain lateral boundary when the waves are three-dimensional (Smith 1980); although in the three-dimensional case, Satomura (1996) has shown that the evaluation of the Reynolds stress along a line, rather than over a plane, can explain its variation with altitude in the steady inviscid case; and
5) the fact that for real and high mountains, the low-level flow goes around the mountain rather than over it, and a large part of the drag is related to low-level flow deceleration (Schär and Durran 1997) rather than to wave emission.

Recent parameterization schemes of subgrid-scale orography in large-scale models account for the last effect (Lott and Miller 1997), this being probably the most important deficit of the preceding schemes, identified using field data. Nevertheless, in this parameterization scheme, the ''wave'' part is still built assuming the hydrostatic approximation and the trapped waves are not considered. In other works (Miller et al. 1989; Lott 1999; Gregory et al. 1998), trapped waves are represented but still in a rather simple way.

To a certain extent, such a simplicity in the treatment of trapped waves in large-scale models hides that the correspondence between the mountain drag and the Reynolds stress is not obvious when they are resonant waves (as noticed Eliassen and Palm 1961, in their seminal paper). Although these waves are evanescent in the vertical direction and above their lowest turning height, they can be an important source of orographic drag (Durran 1995). If these resonant waves are entirely trapped, they carry a significant fraction of the drag in

the horizontal direction only (Bretherton 1969; Lott 1998). If these resonant waves have more than one turning height, they can leak into the stratosphere (Brown 1983) and transport momentum in both horizontal and vertical directions.

To quantify the resonant waves contribution to the momentum balance in a realistic environment, the few airplane data collected during field experiments are helpful because they often reveal trapped waves and allow for the evaluation of the vertical profiles of momentum flux (Bougeault et al. 1993; Hoinka and Clark 1991). A remarkable result is that the general structure of the observed waves, that is, their horizontal wave number and their amplitude variation with altitude, is well predicted by linear steady theory (Vergeiner 1971; Brown 1983; Tannhauser and Attié 1995). Nevertheless, these studies often contradict one with the other when they address the role of the resonant modes in the momentum budget. For instance, Tannhauser and Attié (1995) found that the resonant waves during PYREX do not transfer momentum vertically. Brown (1983), treating the same issue for the British Islands, found that the resonant waves contribute to the Reynolds stress if they leak into the stratosphere and do not contribute to the Reynolds stress if they are trapped.

Following the relative success of the early 2D-linear studies in explaining the airplane data, nonlinear high-resolution nonhydrostatic simulations often reproduce these waves with some realism. Such simulations have been made for various mountain ranges during the last two decades and for different models configurations (linear, nonlinear, 2D, 3D. . .). Among these numerical studies, the most advanced are the 3D high-resolution nonhydrostatic model simulations of real case studies, following the pioneering example of Clark and Gall (1982). For the PYREX experiment, nonlinear 2D simulations have been performed by Elkhalfi and Carrissimo (1993) and Satomura and Bougeault (1994) among others, and nonlinear 3D simulation by Broad (1996), for instance. Again, it is noteworthy that all these simulations give quite realistic trapped waves but often fail in simulating the momentum fluxes.

Without referring to complex nonlinear 3D processes, the fact that models and observed momentum fluxes often differ can have two origins. On the one hand, it can come from the analyses of the airplane data themselves, in the sense that the momentum fluxes they provide may not be as representative as they are usually considered. As an example, in Bougeault et al. (1993), the momentum fluxes' vertical profiles, evaluated with the detrended airplane data, are provided without error bars. Their significance is thus questionable; all the Reynolds stress values given being rather small. On the other hand, it can come from the model studies themselves, and because the resonant modes of the flow and the associated momentum flux vertical profiles are extremely sensitive to small changes in the upstream flow and orography profiles. As an example, if we consider

two slightly different mean flows, the first one can have a resonant mode that is entirely trapped into the low troposphere, while the second one can have a resonant mode that leaks or partially leaks toward the stratosphere. When considering a momentum budget integrated over the troposphere depth, in the steady case, only the first of these two flows has a mode that carries momentum in the horizontal direction only.

The purpose of the present paper is to examine the contribution of lee waves to the momentum budget in a realistic context. For this purpose, we analyze again the airplane data collected during the Pyrénées Experiment (PYREX) and interpret them using linear wave theory. The analysis has much in common with that of Tannhauser and Attié (1995), but, as we shall see, it completes it by discussing modes they did not find and by drawing conclusions rather different from theirs, concerning the contribution of the resonant modes to the momentum budget. In this analysis, we make a spectral and a cross-spectral analysis of the data that has much in common with that of Brown (1983) for the British Isles, but our conclusions differ regarding the contribution of the fully trapped waves to the momentum budget. To gain dynamical realism we then make a limited number of nonlinear dissipative simulations keeping the 2D constraint, and attempt to reproduce the observed waves as well as possible. These simulations indicate that dissipative and nonlinear effects alone cannot explain that a trapped mode can transport momentum if it does not in the linear inviscid case.

Although we suggest that there are some benefits in making again 2D analyses of observed waves, it is important to recall that this approach is not much justified for many flow and orography configurations. Low-level flow splitting for instance (Schär and Durran 1997) is a major difficulty for 2D studies, but the absence of a large-scale pressure gradient and Coriolis force is another one (Bougeault 1994). When there can exist resonant modes, the fact that the mean wind veers with altitude makes that their horizontal wavenumber can be oriented in a direction that differs a lot from that of the low-level flow (Sharman and Wurtele 1983). Because of these processes, the simulations presented here have systematic errors that are discussed with some details. We try to correct some of them by making explicit changes in the models specification. For instance, in the linear model, the simulated waves only resemble the measured one if they are forced by the upper part of the Pyrénées (i.e., forced by what is referred to as its cutoff profile). It is a way to parameterize the impact of low-level flow splitting on the mountain waves' forcing. As another example, we only consider a date where the incident wind does not veer a lot with altitude, so the resonant modes have good chances to be oriented into the dominant direction of the flow.

Section 2 presents a spectral analysis of the airplane data collected above the Pyrénées main transect during the intensive observation period (IOP) 3 of PYREX
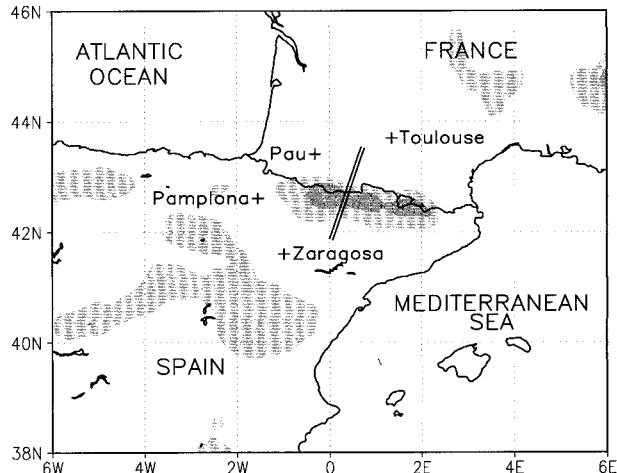

FIG. 1. Smoothed terrain elevation and PYREX data used. Here, + denotes the location of the high-resolution soundings. The two thick lines indicate the airplane paths during the IOP 3. The light- and dark-shaded areas denote terrain elevation above 1000 m and 1500 m, respectively.

(Bougeault et al. 1993). In this analysis, the detection of resonant modes and their contribution to the observed Reynolds stress profile is addressed. Section 3 presents linear simulations of mountain waves in configurations (incident flow, mountain profile) that correspond to the PYREX IOP 3. These simulations allow us to give a simple interpretation of the observed lee-waves structure and to quantify the fraction of momentum they transport in the horizontal direction only. In this section, extensive sensitivity tests are made. In these tests, the background flow specifications are changed within realistic bounds, the build-up phase of the resonant modes is analyzed, and the mountain profile is modified to parameterize nonlinear low-level flow splitting. Section 4 presents fully nonlinear 2D simulations. Section 5 summarizes the results and discusses the implications for the parameterization of gravity waves in large-scale models.

2. Data analysis

a. Description

Among the data collected during the PYREX field experiment (Bougeault et al. 1990), we will use the high-resolution vertical soundings launched from Zaragosa, Pamplona, Pau, and Toulouse. These four stations are located 150 km upstream of the Pyrénées at their upstream foot; and 150 km downstream, at their downstream foot, respectively (Fig. 1). Pamplona and Pau are slightly to the west of the main PYREX transect, Zaragosa and Toulouse are nearly along the transect. These soundings thus provide four relevant high-resolution samples of the background flow. We will also use the airplane data collected above the PYREX main transect extensively.

All along the paper, attention will be focused on the PYREX IOP 3 (1800 UTC, 14 October 1990–1200 UTC, 15 October 1990), when a trough over eastern Atlantic directed south to southeast winds, approximately perpendicular to the Pyrénées ridge. The vertical profiles of the horizontal wind deduced from the soundings, show that the wind direction varies by less 25° between $Z = 3$ km and $Z = 15$ km at 0600 UTC. This is the fundamental reason why 2D studies are more adapted for this date than for the three other PYREX cases during which comparable cross-ridge airplanes' measurements were made. Indeed, when the wind veers with altitude, the vertical profile of the Scorer parameter vary with the angle considered, so that the resonant modes structure can vary with this angle as well (Sharman and Wurtele 1983). During this IOP 3 low-level lee vortices, upper-level and trapped waves have been observed by a large variety of instruments (Benech et al. 1994; Attié et al. 1997). As a signature of these characteristic processes, the pressure drag is large during this period (Bessemoulin et al. 1993).

b. Analysis

The purpose of this analysis is to extract from the airplane data, the dominant oscillations in which wavelengths are above 1 km, typically. To do so, we first detrend the series of vertical velocity, w, horizontal velocity along the transect, u, and potential temperature, θ. We next interpolate them linearly onto a uniform grid of 70 m horizontal resolution. Then, to increase the signal–noise ratio, we filter out the fluctuations with wavelength below 350 m smoothing the data by a 5-point nonrecursive filter for which weights are 1/8 for the two extrema and 1/4 for the three central points. The resulting data are then sampled every 5 points (i.e., every 350 m), in the following, they will be referred to as w', u', and θ', respectively. We verified that this smoothing does affect the spectra at wavelengths above 1 km, and that it does not affect the Reynolds stress. Figure 2 shows the resulting vertical velocity w' for the 10 transects made at different altitudes on 15 October 1990, around 0600 UTC. The lower curve shows the mountain height profile viewed from the airplanes. Figure 2 clearly shows several lee wave trains in the troposphere. The maximum vertical wind amplitude (crest to crest) is about 10 m s^{-1} and is found in the range 3500–5000 m; it is smaller above.

To extract resonant modes from these series, we next evaluate the power spectra of the vertical and horizontal velocity fields w' and u' and of the potential temperature field θ', when the latter is available (for the four lowest flights). The technique used is a conventional Blackman–Tukey correlogram of the series tapered by a 180-km-long Tukey window. To provide error bars on the spectral estimate as well as on the Reynolds stress we model the cumulative effects of measurements errors and of naturally random nonoscillatory fluctuations by
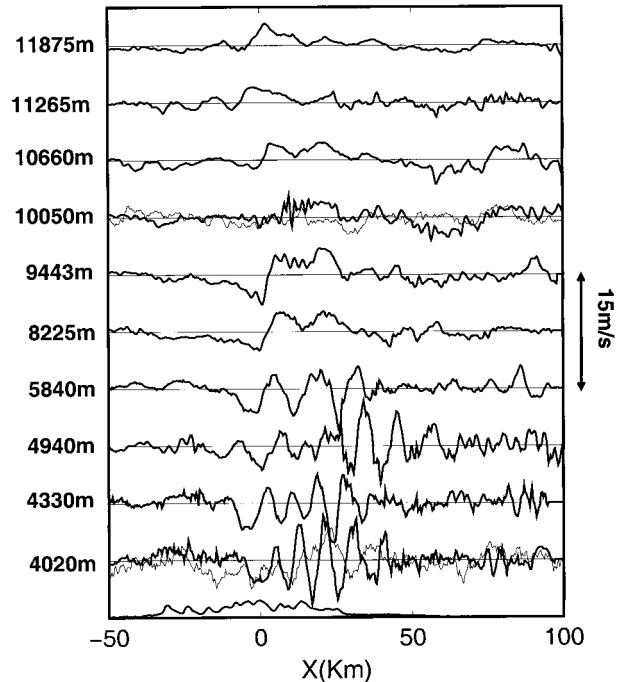

FIG. 2. Observed vertical velocities from different aircraft legs, from 15 Oct 1990 around 0600 UTC. Thick lower curve represents the Pyrénées; the thin curve at the $Z = 4$ km and $Z = 10$ km are red-noise surrogates with characteristics adapted to the measured vertical velocity at that level.

a red noise. This technique is conventional when one wishes to extract oscillations from geophysical series but was not used in the studies of the mountain waves during PYREX. This is rather surprising since it allows us to provide the error bars needed to describe precisely what information can be extracted from the data.

The choice of red noises to test the series is motivated by the fact that the null hypothesis for red-noise tests is that the series does not differ from a 1-order autoregressive process (AR 1), which does not contain oscillations. It also follows that all the power spectra we compute have a median shape that looks like that of a red noise, in the wavelength domain we investigate. For this last purpose, the prefiltering described before is essential. It allows a reduction of the wavelength domain size by a factor of 5: it is easier to approach the median shape of a spectrum by a simple red-noise spectrum when the wavelength domain is short.

To perform the tests, we associate the 24 series of interest (u', w' at the 10 levels, θ' at the far lowest levels) with 24 ensemble of independent AR-1 series whose variance and lag-1 cross-correlation match those of the measured series. These AR-1 series are of the form $Y_{x+dx} = aY_x + Z_x$, where Z_x is a white noise. Two examples of such a series are shown in Fig. 2 at $Z = 4$ km and 10 km, where they are superimposed to the measured vertical velocity. These stochastic series show purely random fluctuations dominated by rather long
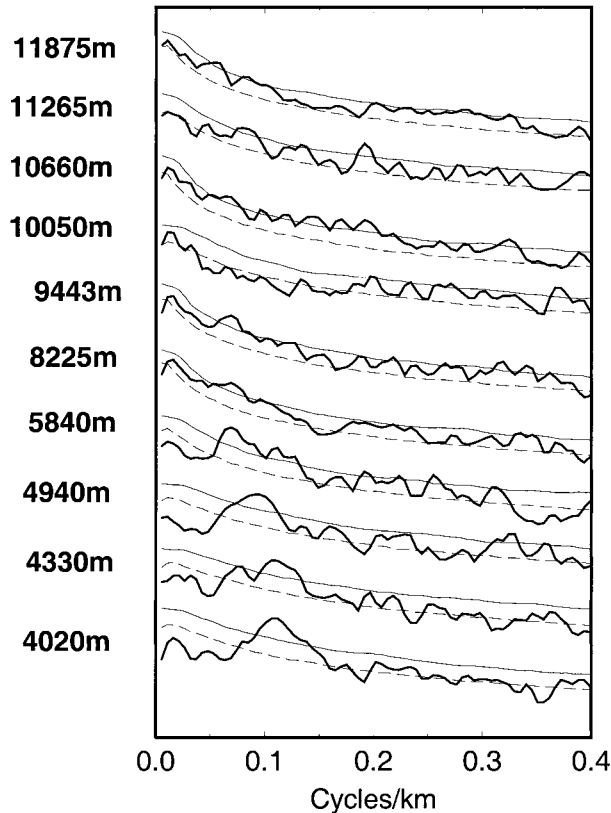
FIG. 3. Power spectra of the vertical velocity fields (heavy solid), median level (light-dashed), and 99% confidence level (light solid). Spectral resolution is 5.3 10^{-3} cycles km^{-1}.

waves, which is a classical behavior of red noises. The fact that such series can look like waves does not disprove the hypothesis that the measured wind contains oscillations, it provides a null hypothesis for what is seen. To test the robustness of the results presented next, we adopt a Monte Carlo procedure, in which all analyses (spectra, cross-spectra, and Reynolds stresses) are compared to analyses done with ensembles of 1000 AR-1 surrogates build as described before. The results are significant if they exceed, in 99% of cases, the values obtained with the surrogates.

The power spectra of the vertical velocity (Fig. 3) at the four lowest levels, show that below $Z = 6$ km the signal is dominated by oscillations with wavelengths ranging from $\lambda_x = 8$ km to 17 km. More precisely, for the two lowest flights, at $Z = 4$ km and $Z = 4.3$ km, the most significant peak is centered at $\lambda_x \approx 8.5$ km. At $Z = 4.9$ km it is around $\lambda_x \approx 10$ km and at $Z = 5.8$ km it is around $\lambda_x \approx 15.5$ km. The fact that at the intermediate level, $Z = 4.9$ km, the wavelength of the most significant peak is in between the values detected above and below follow that the spectral analysis does not allow to separate at this level, the two different oscillations detected at the two adjacent altitudes. That there are two distinct oscillations is further indicated by

the fact that a peak at $\lambda_x \approx 15.5$ km is also significant at $Z = 4.3$ km, and that a peak at $\lambda_x \approx 8.5$ km is significant at $Z = 5.8$ km. For these four flights, the spectra of potential temperature θ' (not shown) give exactly the same results. The cross-spectra between w' and θ' (not shown) shows that both quantities are in quadrature at nearly all wavelengths.

The characteristics of the w'-spectra at the six highest levels change significantly (Fig. 3). At these altitudes the spectra are much redder, which means that the signal is dominated by a continuum of long waves rather than by oscillations with well-defined wavelength: the maxima in the power spectra are nearly always above $\lambda_x = 50$ km, and are never significant. Still, in four of the six upper-level flights, the oscillation with $\lambda_x \approx 15.5$ km is significant. Furthermore, all these six spectra are dominated by a peak around 66–100 km. The fact that these long oscillations hardly pass the 99% test is natural. Indeed, the test is designed to distinguish oscillations above a background noise. Nevertheless, in the theory of mountain waves, the long waves form a continuum of freely propagating modes that are not much amplified or attenuated by the background flow. They thus essentially reflect the spectra of the mountain forcing at wave numbers below the minimum of $[S(z)]^{1/2}$, where $S(z)$ is the Scorer parameter. Since the mountain forcing has a near red spectra at long wavelength (not shown), we can expect the nonresonant response to be red as well. When these long waves dominate the signal, they dominate the design of the test, and it is natural that they do not show up as significant, the test-rejecting signals looking like red noise.

The spectra of the horizontal velocity fields (not shown) are much redder than those of w' at all altitudes reflecting the fact that the u' series has much more power at long wavelengths than at short ones: at all altitudes, the largest peak is always around 66–100 km. Still, marginally significant peaks are found in the four lowest flights at the wavelengths indicated in both the w' and θ' spectra.

To evaluate the contribution of the oscillations to the wave Reynolds stress,

$$\mathrm{Re} = \int_{X_{\min}}^{X_{\max}} \overline{\rho} u' w' \, dx$$

$$= (X_{\max} - X_{\min}) \sum_{k=-\infty}^{+\infty} \overline{\rho} \hat{u}_k \hat{w}_k^*, \qquad (1)$$

we next make a cross-spectral analysis of u' and w'. In Eq. (1) the hats identify the coefficients of the Fourier transforms of the series, and $X_{\max} - X_{\min}$ is the series length. The mean density $\overline{\rho}$ is considered to be consistent with the anelastic form of the Reynolds stress used in the next sections, but we verified that the density disturbances are small enough that they can be neglected in the Reynolds stress evaluation.

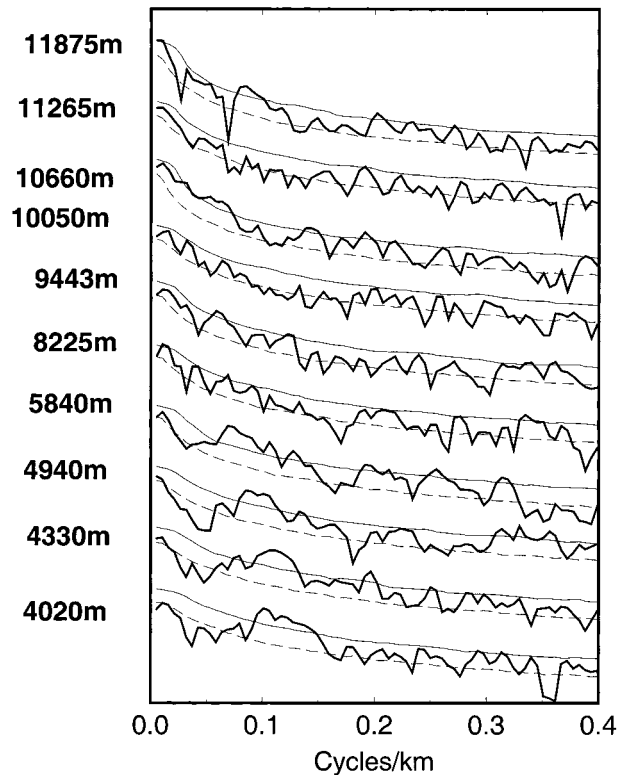Figures 4 and 5 show the amplitude and phase of the

FIG. 4. Coherence of the cross-spectra between the horizontal and vertical velocity fields (thick solid), median (thin-dashed), and 99% confidence level (thin solid). Spectral resolution is 5.3×10^{-3} cycles km^{-1}.

FIG. 5. Phase of the cross-spectra between the horizontal and vertical velocity fields. Phase (filled square). Spectral resolution is 5.3×10^{-3} cycles km^{-1}.

cross-spectra, respectively. As found in the vertical velocity spectra, the trapped waves are the only ones for which contribution to the cross-correlation can be extracted significantly. The phase of the cross-spectra show that at $Z = 4$ km and $Z = 4.3$ km the vertical and horizontal velocity fluctuations associated with the oscillations, with wavelength around 10 km, are out of phase (they are of opposite sign) and give a negative Reynolds stress. At higher levels ($Z = 4.9$ km and $Z = 5.8$ km), the coherence is still significant for disturbances with wavelength around $\lambda_x \approx 10$ km (Fig. 4) but the horizontal velocity fluctuations are more in quadrature, the trapped waves contribute less to the Reynolds stress than below. The explanation for this is that the 7–15-km waves become evanescent in the vertical direction as the altitude increases, because the Scorer parameter decreases with altitude. To interpret the coherence and phase spectra at a small horizontal wavenumber is more problematic, since significant contributions are hardly found. Still, at the five highest levels, the cross-spectra have marginally significant peaks above 50 km wavelength, indicating that the u' and w' fields vary with more coherence than two independent random series. At all levels, the vertical and horizontal velocity fluctuations at small horizontal wavenumbers are essentially out of phase, thus giving a negative con-
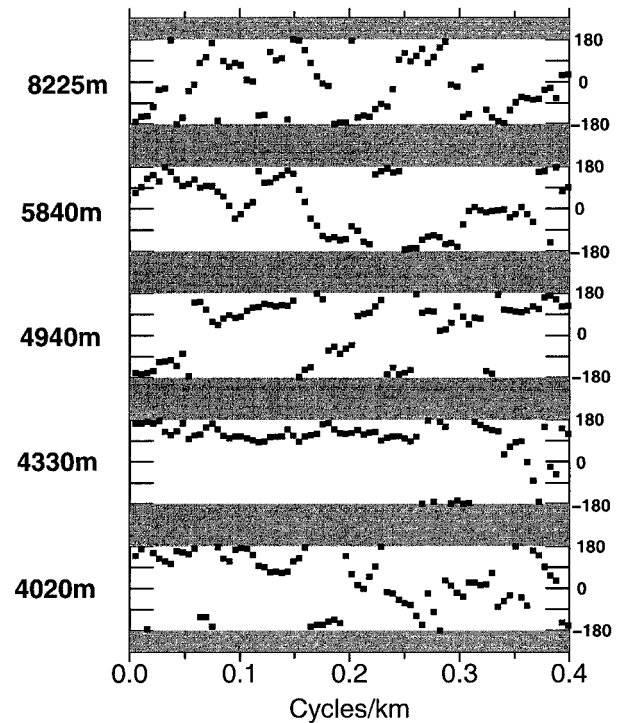
tribution to the Reynolds stress. Furthermore, above 6 km, the largest contribution to the cross-spectra comes from the long waves.

Figure 6a shows the vertical profile of the integrated Reynolds stress (1), together with 99% confidence intervals evaluated by a Monte Carlo procedure using the AR-1 surrogates of both the u' and w' series. Since the u' and w' surrogates are build independently from one another, their theoretical cross-correlation is zero. The size of the confidence interval illustrates well the limit of using finite length series to compute the stress: the spreading of the surrogate stresses is such that there is no altitude where the stress computed with the measured data is significant. Nevertheless, this test is extremely conservative, because the AR 1 series fit the complete series, while according to the spectral and cross spectral analysis shown before, part of the measured signals can be attributed to well-defined oscillations.

To evaluate the contribution of these oscillations to the Reynolds stress and to exclude them from the design of the statistical test, we next filter the observed series using two low-pass filters with a Kayser window (Hamming 1983) whose parameters are adjusted to avoid Gibbs effects (for a more complete description of the filter see Scavuzzo et al. 1998). The first filter suppresses the disturbances with horizontal wavelength lower than 5 km the second one suppresses wavelengths lower than 25 km. The choice of the 5-km and 25-km cutoffs is based on the fact that the oscillations detected previ-
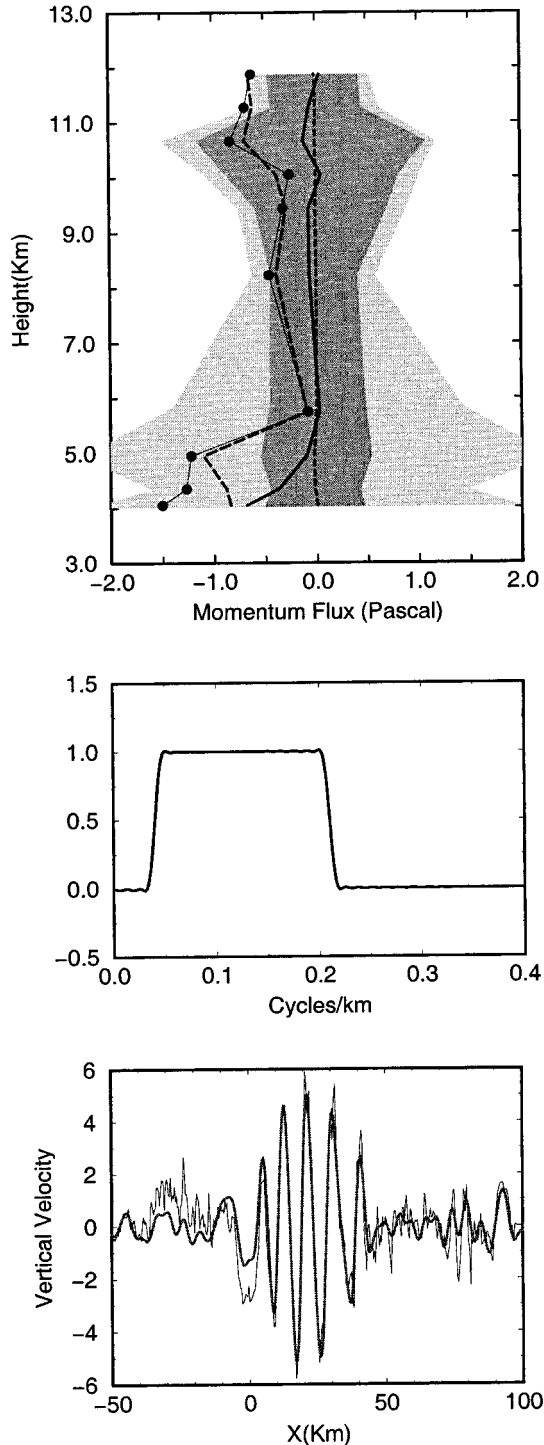
FIG. 6. (a) Reynolds stresses: raw data (solid and circle), 5–25 km bandpass (thick solid), $\lambda_x < 5$ km (thick-dashed), $\lambda_x > 25$ km (thick long-dashed), 99% confidence (light-shaded), and 99% confidence with 5–25 km waves excluded from the test (dark-shaded). All values are in pascals; that is, Re in Eq. (1) is divided by the length $L = 110$ km—typical of the pathlength along which the mountain drag is measured. (b) Transfer function associated to the 5–25 km bandpass filter. (c) Comparison between bandpassed (thick) and raw (thin) vertical velocities at $Z = 4$ km.

ously in the series have wavelengths in between these values. The choice of the 25-km cutoff is also motivated by the fact that waves with wavelengths larger than 25 km, essentially propagate freely toward the low stratosphere.

In the following we will use the difference between the complete series and the 5-km low-pass series to evaluate the contribution of the disturbances with wavelength smaller than 5 km to the Reynolds stress. We will use the 25-km low-pass series to evaluate the contribution of the "long" freely propagating waves to the stress. The 5–25-km series, build as the difference between the 5-km low-pass series and the 25-km low-pass series will be used to evaluate the contribution of the resonant modes to the stress. The transfer function associated with this bandpass procedure is displayed on Fig. 6b, and a comparison between the full signal and the 5–25-km signal is shown on Fig. 6c. Figure 6c shows that the bandpass vertical velocity oscillations compare well with those observed in the raw series: the 5–25-km series contains the resonant modes.

Since the oscillations that dominate the 5–25-km series have been detected without ambiguity in the spectral analysis, we can assume that the 5–25-km waves are not part of the noise. We thus build new series of surrogate AR-1 series that matches the measured signal minus the 5–25-km signal and deduce the 99% significance levels accordingly (dark-shaded in Fig. 6a). According to these new confidence intervals the Reynolds stress values can be considered different from zero at the three lowest levels and at $Z = 8.2$ km, 11.2 km, and 11.8 km (solid and circles, Fig. 6a). According to these new confidence levels, in the lower part of the Reynolds stress profile (below 6 km) the contribution of the trapped waves is essential (thick solid in Fig. 6a): they are associated to a stress of less than -0.7 Pa at the lowest level, which corresponds to a little less than half the total Reynolds stress value. As altitude increases, the stress due to the trapped waves drops sharply, consistent with that the w' and u' field becomes more in quadrature as altitude increases (Fig. 5). The thick-dashed line in Fig. 6a also shows that the disturbances with wavelength shorter than 5 km do not participate to the Reynolds stress. The thick long-dashed line in Fig. 6a shows that the disturbances with wavelength longer than 25 km contribute to the stress at nearly all levels. At ground level, the long wave contribution is close to that of the trapped modes and stay near Re = -1 Pa up to 5 km. If one excludes from the discussion the altitude $Z = 5.8$ km, at the six highest levels, the Reynolds stress due to the long waves is not much different from that. Indeed, it is again near Re = -1 Pa at $Z = 10.6$ km, 11.3 km, and 11.8 km. It is larger than that but does not goes above Re = -0.3 Pa at $Z = 8.2$ km, 9.4 km, and 10 km. Since the confidence interval in Fig. 6a is 1-Pa large, it is statistically correct to say that, except at level 1, the values of the stress due the

long waves at all levels is nearly that due to the resonant modes at the lowest level.

Extensive sensitivity tests to the bandpass filter window have also been made. They show that the results above are not very sensitive to the window definition, providing it includes the 8–20-km band, that is, that the bandpass signal contains the two oscillations detected in the above spectral analysis. We also computed the Reynolds stresses related to wavelengths between 8 km and 13 km on the one hand, and between 13 and 20 km on the other. Although the values become too small to be significant, we found that each of these two bands have nonzero momentum fluxes of comparable amplitude at the two lowest levels.

3. The linear nature of the trapped waves

a. Model description

All of the following results have been obtained using the anelastic approximation (Lipps and Hemler 1982; Scinocca and Shepherd 1992). In this approximation, freely propagating gravity waves and trapped mountain waves coexist and the equations of motion form an Hamiltonian system in the isentropic nonviscous context (i.e., a system from which wave activity conservation laws can be deduced). The 2D linear equations that result from the anelastic approximation are (see for instance Lott 1998):

$$(\partial_t + U\partial_x)\omega' - \left(\frac{\Omega}{\rho_0}\right)_z \partial_x\psi' - c_p\frac{d\pi_0}{dz}\partial_x\theta' = 0, \quad \text{and} \quad (2)$$

$$(\partial_t + U\partial_x)\theta' - \frac{N^2\theta_0}{g\rho_0}\partial_x\psi' = 0; \quad (3)$$

and the linear lower boundary condition is,

$$\psi'(0) = -\rho_0(0)U_0h(x) \text{ at } Z = 0. \quad (4)$$

Here, U, Ω, ρ_0, π_0, and θ_0 are the background state (uniform in the horizontal direction) horizontal wind, vorticity, density, Exner pressure, and potential temperature respectively, and h is the terrain elevation. Also, ω', ψ', and θ' are the disturbance vorticity, streamfunction, and potential temperature associated with the perturbation respectively. In Eq. 4,

$$U_0 = \frac{1}{h_{max}}\int_0^{h_{max}} U(z)\,dz$$

characterizes the incident wind intensity that hints the ridge, h_{max} being the maximum terrain elevation.

The linear wave field is evaluated using a time-dependent numerical model that is close to the one used by Wurtele et al. (1987) or by Lott and Teitelbaum (1993). It solves Eqs. (2) and (3) in spectral space in the horizontal direction and in finite-differences in the vertical direction. In all the linear simulations, the total domain height is 30 km, its length is 600 km, and the
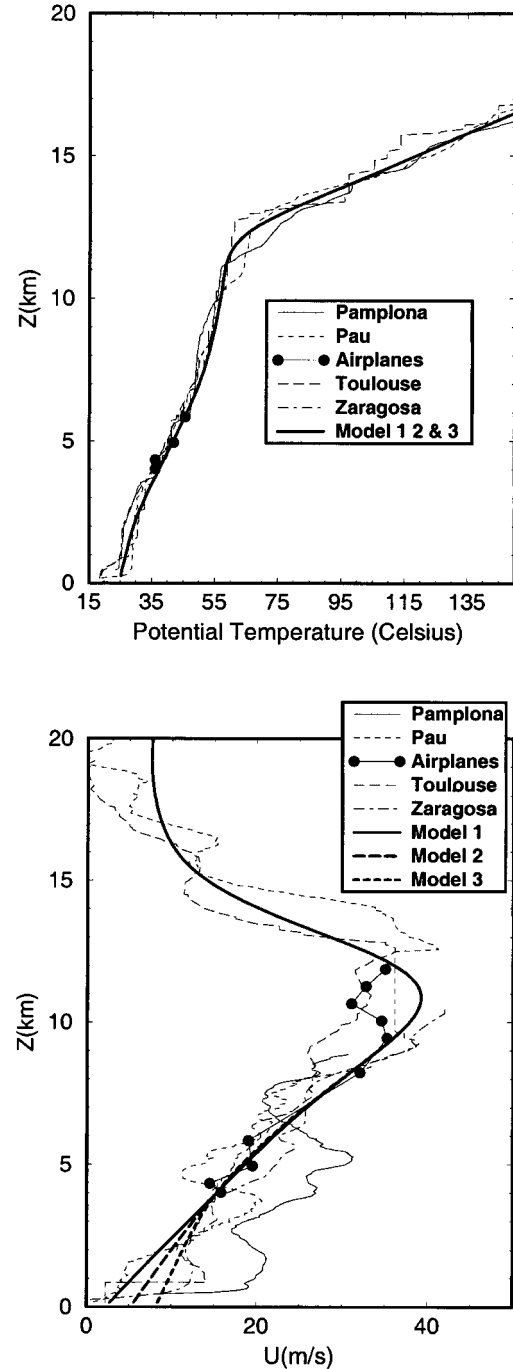

FIG. 7. Flow profiles the 0600 UTC 15 Oct 1990 measured by high-resolution soundings, airplanes, and background profiles used in the linear model simulations: (a) potential temperature and (b) horizontal wind.

lateral boundary conditions makes the wave field periodic. Furthermore, linear dampings are introduced (Rayleigh friction and Newtonian cooling) on the right-hand side of Eqs. (2) and (3) to define sponge layers at the leeward and upward boundaries of the model domain. The length of the leeward sponge layer is equal
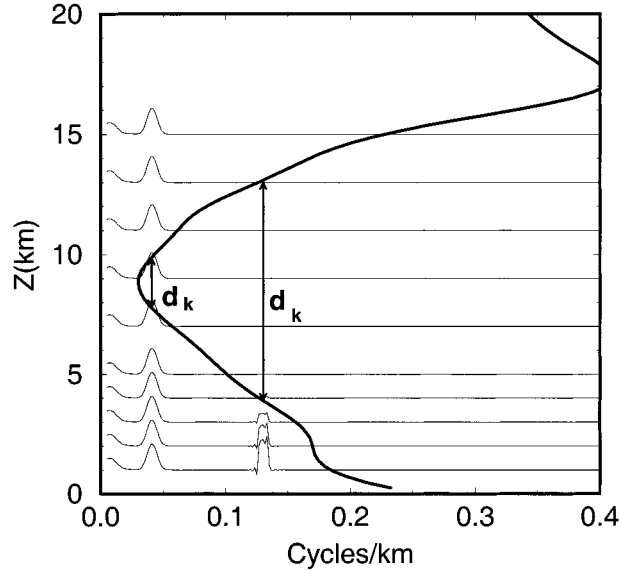
FIG. 8. Steady linear simulation. Here, $[S(Z)]^{1/2}$ (S is the Scorer parameter) for the smoothed-incident flow profile 2 (thick solid), and contribution of each harmonic to the Reynolds stress at at $Z = 1, 2, 3, 4, 5, 7, 9, 11, 13,$ and 15 km (thin solid). Resolution is 8×10^{-3} cycles km^{-1}.

to 50 km, and the depth of the upward sponge layer is 10 km. The amplitude of the dampings was adjusted to minimize backward wave reflections and to maximize absorption. In the cases presented, the model resolution is $dz = dx = 0.5$ km, and for this resolution, model convergence was verified comparing the results to those obtained with $dz = 0.25$ km $= dx/2$ on the one hand, and to those obtained when increasing the domain length to 800 km leaving dx unchanged (i.e., this increases the spectral resolution) on the other. Each simulation begins with a spinup of 1 h, during which the mountain height increases toward its final shape and lasts 72 h to ensure that a steady state is achieved.

The design of the linear model implies that the incident flow profiles U and θ_0 need to be specified together with their derivatives, U_z, U_{zz}, and θ_{0z}. In the linear model this is done by building the profiles of $U(z)$ and $\theta_0(z)$ using few piecewise linear profiles, smoothly linked by hyperbolic tangent functions. They are displayed in Figs. 7a,b, together with the profiles issued from the four high-resolution soundings and with the profiles built by averaging the raw series of u and θ measured by the airplanes. Figure 7 shows that the analytical profiles match quite well those measured.

For the wind, three analytical profiles were tested and compared (Fig. 7b). They differ only below 5 km, in that each smoothly matches three different values of the wind at the ground, $U(0) = 2$ m s^{-1}, 5 m s^{-1}, and 8 m s^{-1} respectively. These profiles are used to test the sensitivity of the wave response to the background flow specification, when we stay within realistic bounds. Many other configurations have been tested, like chang-

ing the maximum wind amplitude or the low-level stratification still within reasonable bounds. None of these modifications gives changes much more pronounced than those occurring when the low-level wind is changed, and there is little benefit in presenting results for more than these three profiles. The topography height in the model has been slightly modified from that measured by the airplane flights. It is lowered to insure an equal altitude on both sides of the 2D model domain.

b. Results

In this section, we often describe the wave field in terms of Fourier series in the horizontal direction. At each altitude and at each time, the Fourier coefficients of each dynamical field is the direct output of the numerical model, which is spectral in the horizontal direction. In the steady case, this description is very natural because one harmonic,

$$\psi_k'(x, z) = \rho_0^{1/2} \Re[\hat{\psi}_k(z)e^{ikx}], \qquad (5)$$

has a vertical structure that is simply governed by the Taylor–Goldstein equation,

$$\frac{d^2\hat{\psi}_k}{dz^2} + \left(\frac{N^2}{U^2} - \frac{U_{zz} - \dfrac{\rho_{0z}}{\rho_0}U_z}{U} + \frac{\rho_{0zz}}{2\rho_0} - \frac{3}{4}\frac{\rho_{0z}^2}{\rho_0^2} - k^2 \right)\hat{\psi}_k$$

$$= \frac{d^2\hat{\psi}_k}{dz^2} + [S(z) - k^2]\hat{\psi}_k = 0, \qquad (6)$$

where $S(z)$ is the Scorer parameter. Near the ground the vertical wavenumber of a harmonic is, $m_k^2(0) = S(0) - k^2$. It corresponds to a vertically propagating wave if the horizontal wavenumber is below $[S(0)]^{1/2}$.

The contribution of each harmonic to the Reynolds stress at different altitudes, $\rho_0(z)\hat{u}_k\hat{w}_k^*(z)$, and the Scorer parameter for the wind profile 2 $[U(0) = 5$ m s$^{-1}]$ are displayed in Fig. 8. The Reynolds stress below 3 km (lowest three solid lines in Fig. 8), is transported by two well-defined harmonics with wavelengths $\lambda_x \approx 7.8$ km and $\lambda_x \approx 24$ km on the one hand, and by a continuum of long modes with $k < k_{min} = \min[S(z)]^{1/2}$ on the other. These two modes are the two resonant modes of profile 2, each contributes equally to the Reynolds stress near the ground, and each transports approximately as much momentum as the continuous part of the wave spectrum.

As altitude increases, the contribution of the short-trapped mode to Re decreases (Fig. 8); it is near zero above $Z = 4$ km, which is also its lowest turning height. In the following such a mode will be referred to as a resonant-trapped mode. Conversely, the contribution of the long-resonant mode to Re stays near constant as altitude increases. As its horizontal wavenumber, $k > [S(z)]^{1/2}$, between $Z = 7.5$ km and $Z = 10$ km, this modes nearly entirely leaks through a zone where it is evanescent according to Eq. (6). In the following such a mode will be referred to as a resonant leaking mode.
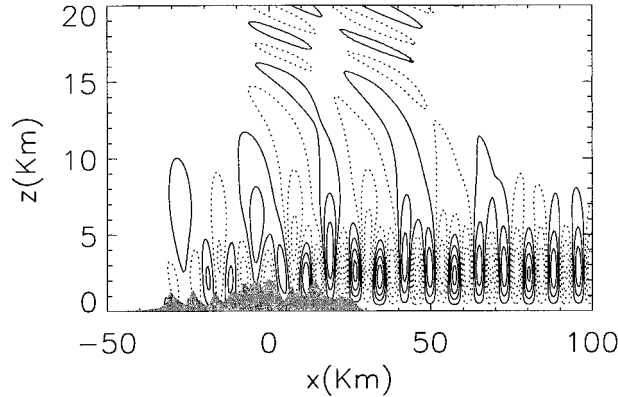
FIG. 9. Linear simulation: vertical velocity field. Contours every 5 m s^{-1}; negative values are dashed.

That the shortest mode does not leak compared to the long one can be easily understood, comparing a characteristic e-folding scale, $l_k^{-1} \approx (k^2_{min} - k^2)^{1/2}$ to the depth over which these modes are evanescent, d_k (which can be taken as the distance between its two turning heights; Fig. 8). For the leaking mode, $l_k = 38$ km $\gg d_k = 2.5$ km, while for the trapped mode, $l_k = 8$ km $\approx d_k = 9$ km.

Figure 9 presents the simulated vertical velocity field and shows a strong lee wave patterns with horizontal wavelength $\lambda_x \approx 7$–8 km below $Z = 5$ km and near $\lambda_x = 25$ km everywhere above, including the stratosphere. Figure 9 further indicates the clearest deficit of the simulation. When compared to Fig. 2, it can be easily seen that the simulation overstates the wave's amplitude and the downstream extent of the waves.

This simulation has to be contrasted to that of Satomura and Bougeault (1994), which, in the same situation, produced waves with small horizontal wavelength through nonlinear interaction; the mountain profile they used being very smooth. In our simulation, the mountain profile directly forces the resonant modes of the background flow. This linear simulation has some points in common with those presented in Lott (1998), since most of the harmonics forced at the ground propagate vertically and encounter a turning height in the troposphere. In contrast with this author nevertheless, all the resonant modes found here have a second turning height so they can eventually leak through the jet stream toward the stratosphere. Nevertheless as the short-resonant mode is trapped, one can expect that a significant part of the wave drag is transported in the horizontal direction only. To address this point, we conduct the pseudo-momentum budget diagnostic made in Lott (1998), and which are a direct application of the theoretical studies about wave propagation and wave-mean flow interaction (McIntyre 1980; Shepherd 1990; Scinocca and Shepherd 1992; Durran 1995). By considering momentum and pseudo-momentum budgets over a rectangular domain $[0, Z]x[-X, +X]$, one can show that the waves Reynolds stress,

$$\text{Re}(X, Z) = \int_{-X}^{X} \rho_0 u'w' \, dx \approx \int_{-X}^{X} F_z(x, Z) \, dx$$

$$= P_z(X, Z), \quad (7)$$

where F_z is the vertical component of the pseudo-momentum flux $\mathbf{F}$. Over this domain, if A is the pseudo-momentum, its budget writes,

$$\frac{\partial M(X, Z)}{\partial t} + [P_z(X, z)]_0^Z + [P_z(x, Z)]_{-X}^{+X} = 0, \quad (8)$$

where the integrated pseudo-momentum $M(X, Z)$, and lateral pseudo-momentum flux $P_x(x, Z)$, are given by,

$$M(X, Z) = \int_0^Z \int_{-X}^{+X} A(x, z) \, dx \, dz \quad \text{and}$$

$$P_x(x, Z) = \int_0^Z F_x(x, z) \, dz, \quad (9)$$

respectively. In the steady case one can show that the drag $D = \text{Re}(X, 0)$; so when there is no wave upstream, $P_x(-X, Z) \approx 0$, and

$$D = P_x(X, Z) + P_z(X, Z), \quad (10)$$

Figure 10a shows that the Reynolds stress decreases with altitude in the trapped layer (i.e., below the turning height of the trapped resonant mode, $Z = 4$ km) whereas it is constant above. Its value at the ground, D, is 1.5 times its value in the constant part of the profile. Since the waves are steady and are not dissipated, this decrease with height of the Reynolds stress can only be balanced by an incoming flux of pseudo-momentum P_x. As shown in Fig. 10b, this horizontal flux is quite large and accounts for more than 33% of the wave drag $D = \text{Re}(Z = 0)$: it exactly balances the increase with height of the wave-Reynolds stress shown before, and closes the pseudo-momentum budget equation in the steady case $D = P_x + P_z$.

c. Sensitivity to the background flow

The differences between the profile of $U(z)$ and $\theta_0(z)$ measured by the soundings and the airplanes (Fig. 7) make the choice of one particular flow to interpret the observed waves rather arbitrary. Indeed, sensitivity tests to these profiles reveal that the wave's structure varies a lot between experiments where the background profiles are modified within limits provided by the extrema of $U(z)$ and $\theta_0(z)$ given by the soundings. To illustrate this point, we present now two-simulations with the profiles 1 and 3 shown in Fig. 7b.

Figures 11a and 11b present the cross correlation $\rho_0(z)\hat{u}_k\hat{w}_k^*(z)$ for profiles 1 and 3, respectively. A noticeable result is that, with profile 1 there are two resonant modes, while with profile 3, there is only one [the local maxima that appears near $k_{min} = \min[S(z)]^{1/2}$ in Fig. 11b is a local maxima of the orography spectrum].
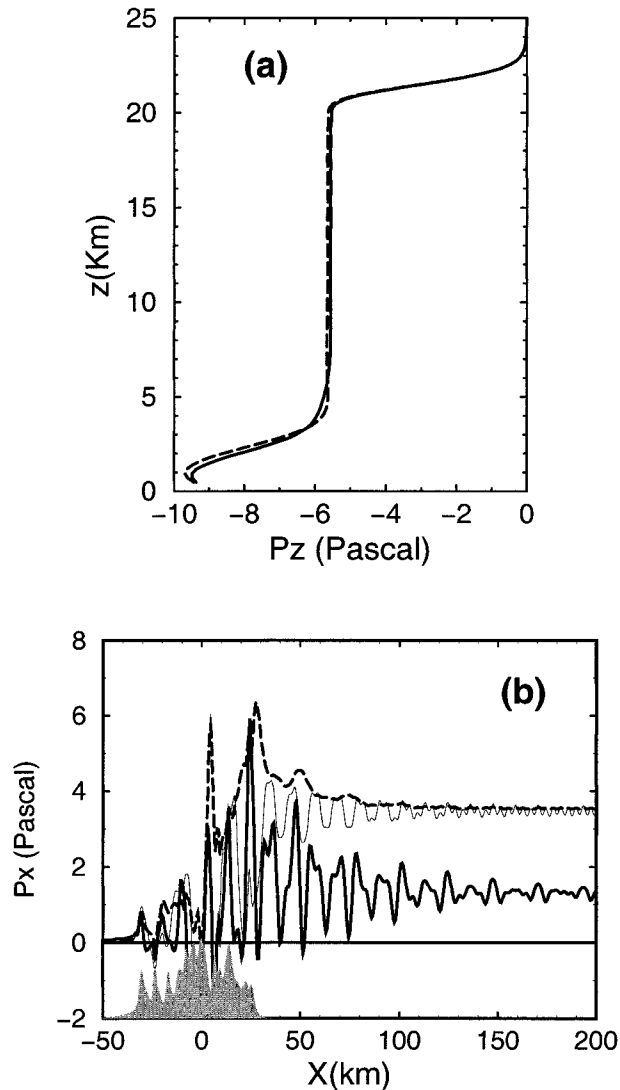
FIG. 10. Linear simulation: pseudo-momentum fluxes diagnostics. (a) The vertical profile of the wave-Reynolds stress; domain half length—$X = 70$ km (thick solid), and $X = 140$ km (thick dashed). (b) The horizontal variation of pseudo-momentum integrated through vertical boundaries of different elevations—$Z = 2.5$ km (thick solid), $Z = 5$ km (thin solid), and $Z = 7.5$ km (thick-dashed). All values are in pascals; that is, P_Z and P_X in Eqs. (7) and (9) are normalized as Re is in Fig. 6a.

FIG. 11. Same as Fig. 8 but for the (a) U profile 1 and (b) U profile shown in Fig. 7.

For profile 1, the shortest mode is entirely trapped and the long one is leaking into the stratosphere. Note nevertheless that the long mode only leaks partially, part of its momentum flux does not pass in the lower stratosphere. Comparing the wave's structure, it is noteworthy that the horizontal wavenumber of the resonant modes are very different from one case to the other. The strongly trapped mode's wavelengths are $\lambda_x = 6$ km, 7.8 km, and 8.9 km for profiles 1, 2, and 3, respectively, those of the leaking modes are $\lambda_x = 13.3$ km and 25 km for profiles 1 and 2, respectively.

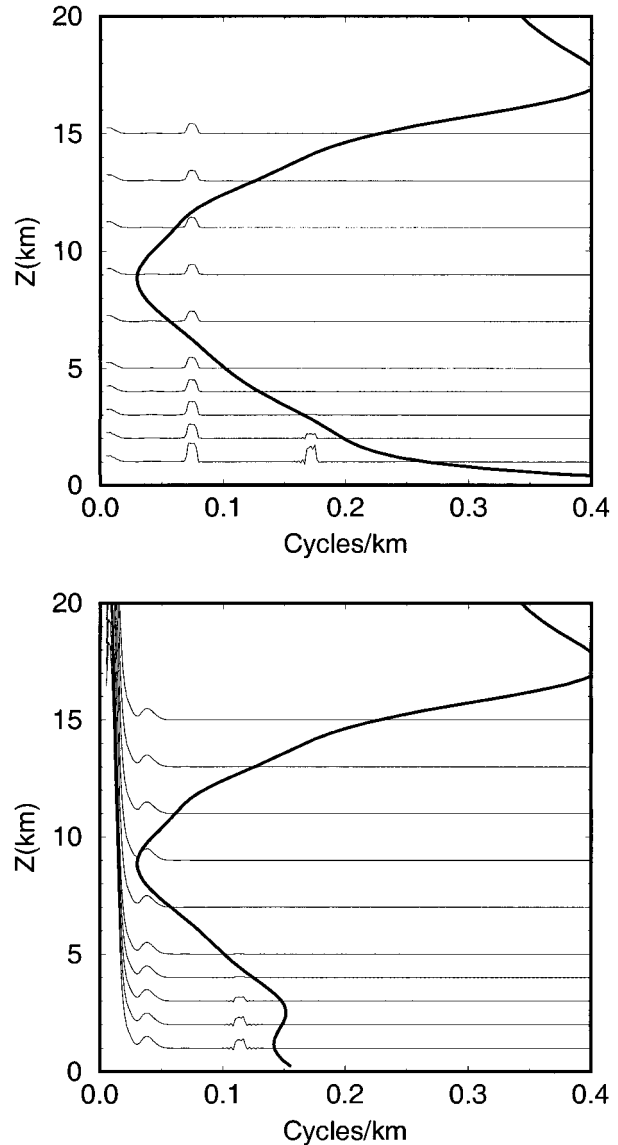The Reynolds stress profiles for these three simula-

tions are presented in Fig. 12a. With a partially leaking resonant mode and a trapped one (U profile 1; thick-solid line in Fig. 12a), the Reynolds stress increases with altitude up to $Z = 6$ km, which is the altitude of the long-resonant partially leaking mode lowest turning height. With a fully leaking long resonant mode (i.e., U profile 2, thick-dashed line in Fig. 12a) the stress only increases up to $Z = 3$ km, which is the altitude of the short fully trapped mode turning height. Note that with profile 3 (thick long-dashed, Fig. 12a), the Reynolds stress is near constant with altitude because (i) the fully trapped resonant mode amplitude is very small, its wavelength being near a zero of the orography spectrum (not shown), and (ii) its constant phase lines are nearly
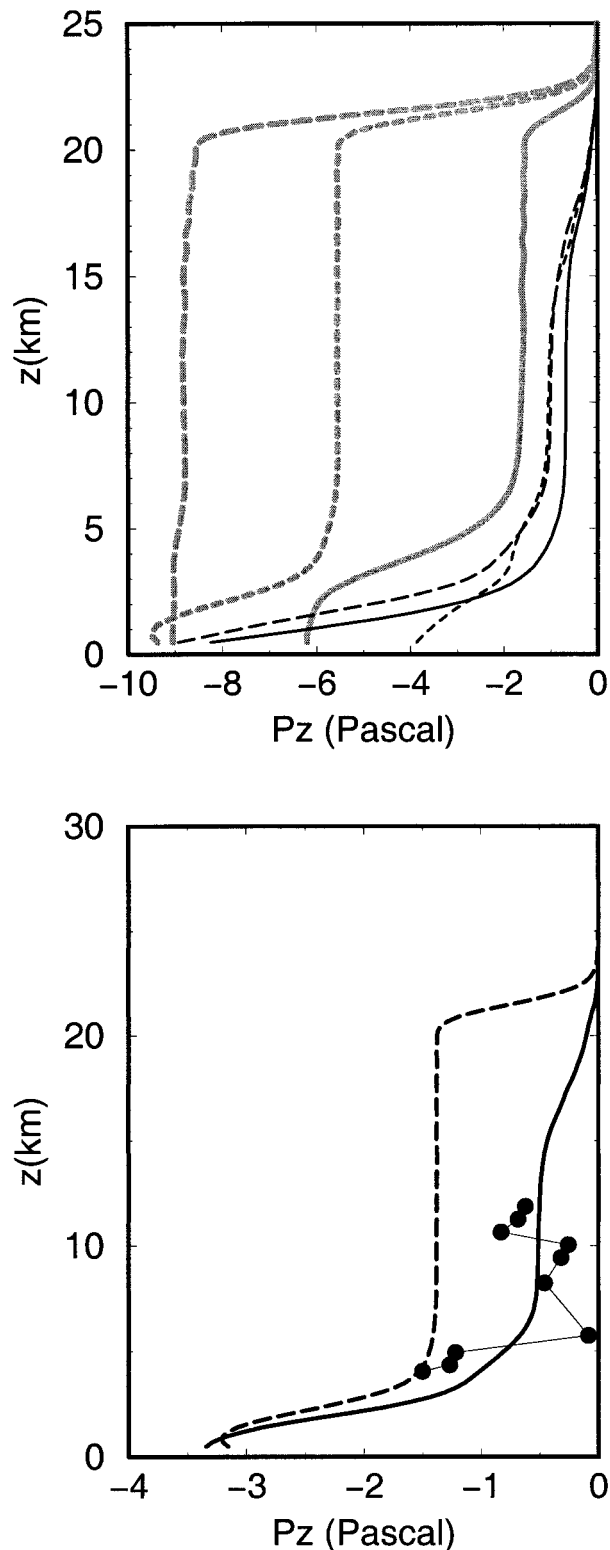
FIG. 12. Reynolds stress profiles for different simulations. (a) Full orography: steady profiles are thick and gray, unsteady ones (3-h run) are thin and black; U profile 1 (solid), U profile 2 (dashed), and U profile 3 (long-dashed). (b) Unsteady simulation with cutoff mountain; U profile 2 model: 3 h (thick solid), 72 h (long-dashed), and airplane data, (thin and circles).

vertical near the ground, its horizontal wavenumber k being near $[S(0)]^{1/2}$.

The point (i), raised by the simulation with the $U(z)$ profile 3, reveals that the linear simulations are extremely sensitive to the orography specification. In the present study the orography is that seen by the lowest airplane flight and probably mixes into a 2D section narrow fully 3D peaks with more 2D-like ridges. Accordingly, we could have constructed the orography profiles in a more consistent way, for instance by averaging in the transverse direction a 3D high-resolution dataset. As there are a lot of arbitrary choices in proceeding so, and as the results obtained would have been qualitatively comparable to those presented here, it seems simpler to proceed as we did. Nevertheless, to emphasize that large quantitative differences are to be expected when the orography spectrum is changed in a moderate way, we have repeated the simulations with profile 3 using a distorted orography profile whose power spectrum is enhanced near the resonant wavelength. This is done crudely by enhancing the orography Fourier coefficients of $h(x)$ in the model by a factor of five within a narrow wavelength band of length 6×10^{-3} cycles km^{-1} centered on the resonant mode horizontal wavenumber, k_x = 0.113 cycles km^{-1}. As a result of this, the orography profile $h(x)$ (not shown), is not much different from the one used before. They differ everywhere by less than 200 m and have the same summits at the same places. In the simulations with this distorted orography, the trapped mode in the steady case transports up to 25% of the Reynolds stress instead of near 0% in the preceding simulations.

d. Unsteady case, cutoff mountain

When compared to airplane data, the steady simulations always overestimate the wave amplitude and the downstream extent of the resonant trapped modes. Without referring to three-dimensional and/or dissipative processes, these errors can be related to the fact that the observed waves are unsteady or that the dynamic is nonlinear. According to the strong sensitivity of the waves to the background flow specification, the steady hypothesis is not much justified because the resonant modes take a long time (more than a few hours) to build themselves a few tens of a kilometer downstream of the ridge. It is difficult to believe that in a realistic context, the Scorer parameter remains the same for more than a few hours. As an indication of this, we analyzed the variation in time of the minimum value of the Scorer parameter deduced from the soundings. At 0600 UTC it was around 0.03 km^{-1} (Fig. 8) while 6 h before, it was around 0.05 km^{-1}. This difference is due to the fact that the maximum wind perpendicular to the ridge has rapidly increased during this period.

To address this unsteady aspect, we present here the results of the experiments described in sections 3b and 3c after 3 h of integration only. At this time, the model

response presents only few oscillations downstream of the ridge (not shown), which is more consistent with the number of oscillations detected by the airplanes in Fig. 2. For the Reynolds stress profiles (thin lines in Fig. 12a), these simulations reveal that all the resonant modes (trapped, partially leaking, or fully leaking) contribute to its amplitude decay with altitude below $Z = 7$ km, typically. For the leaking modes, this effect follows that the pseudo-momentum A above the ridge and at low-level decreases in time during the build-up phase. Since the lateral fluxes of pseudo momentum $F_x(X, Z)$ in Eq. 8 are negligible at $t = 3$ h, and for $X > 50$ km, the variations in time of the integrated pseudo-momentum M can only be balanced by a Reynolds stress that increases with altitude.

The deficit of the linear model in simulating the wave amplitude is probably related to 3D nonlinear low-level flow splitting. Indeed, for the PYREX IOP 3, the non-dimensional mountain height H_N is larger than 1:

$$H_N = \int_0^{h_{max}} \frac{N}{U} \, dz \approx 3 \gg 1,$$

where h_{max} is the maximum of the mountain profile shown in Fig. 2, and $N(Z)$ and $U(z)$ are those of profile 2. This means that the overall dynamics is not linear (see for instance Smolarkiewicz and Rotunno 1989) so that an important fraction of the flow below h_{max} passes around rather than over the mountain. To estimate that fraction, we follow Lott and Miller (1997) and calculate the blocking level height Z_b:

$$\int_{Z_b}^{h_{max}} \frac{N}{U} \, dz \approx 1.$$

This relationship gives, $Z_b = h_{max} - 1000$ m for profile 2. Next, assuming that only the fraction of air located between Z_b and h_{max} passes over the mountain and excite waves, we assume that the incident flow only see's a mountain that is $h_{max} - Z_b$-high, and for which the profile is that of the Pyrénées peaks that exceed Z_b.

Linear simulations with this cutoff mountain have been conducted with U profiles 1, 2, and 3. In the steady case, they systematically show better agreements with the observations regarding both the wave amplitude and the Reynolds stress compared to the cases with full orography. For the number of oscillations downstream of the ridge they again need to be looked at after only 3 h of integration to resemble the measured fields. An example is given in Fig. 13, which shows the wave field after 3 h for an integration forced by the cutoff orography (lowest curve in Fig. 13) and for wind profile 2. The agreement with observation is reasonable at all altitudes, and the Reynolds stress presents a variation with height up to 6–7 km (Fig. 12b). In this simulation, the analysis of the contribution of each harmonic to Reynolds stress, shows that the amplitude decay of Re with altitude in Fig. 12b is in part due to the buildup of the resonant modes but is also due to the buildup of the long non-
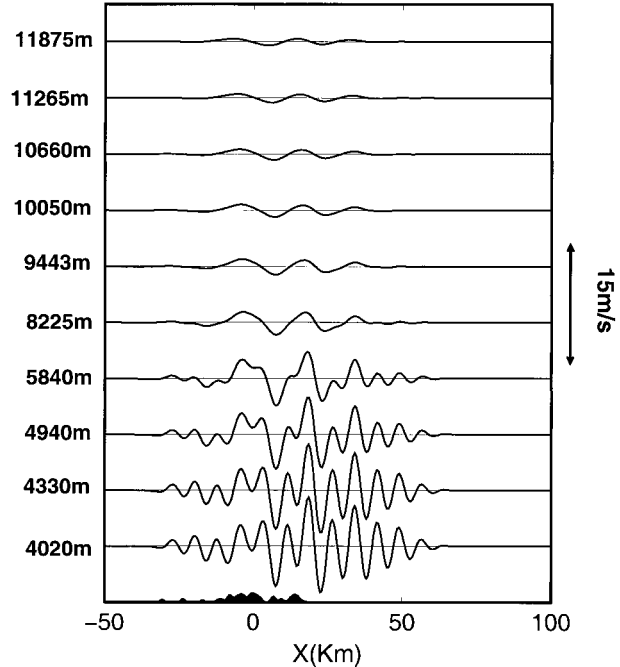

FIG. 13. Unsteady linear simulation (3-h run) with cutoff orography and U profile 2. Vertical velocity at airplane flight transects.

resonant waves. This last result is also consistent with the observations, the amplitude of the stress due to the long waves (thick long-dashed line in Fig. 6a) being larger below 5–6 km than above.

4. Nonlinear dissipative effects

This last linear simulation reveals two important ingredients needed to simulate with accuracy the amplitude of the lee-waves system: the nonlinearities, and especially the fact that a significant fraction of the incident flow goes around instead of passing over the ridge and the fact that the observed waves are unsteady. They also reveal that if the difference $S(0) - \min[S(z)]$ is "small" (as for profile 3), the contribution of the resonant modes to the Reynolds stress can be small. If this is the case in nature, it means that the contribution of the trapped modes to the stress is due to processes not accounted for in the linear simulations, like the nonlinearities and the dissipations. To address these points, we next conduct a limited series of nonlinear simulations for a given flow profile where the difference $S(0) - \min[S(z)]$ is as small as in profile 3. We then adjust dissipation in the model to again match the observations as well as possible.

a. Model description

The model used is the mesoscale nonhydrostatic (meso-NH) model (Lafore et al. 1998) with an integration domain of length 320 km and of height 20 km. The
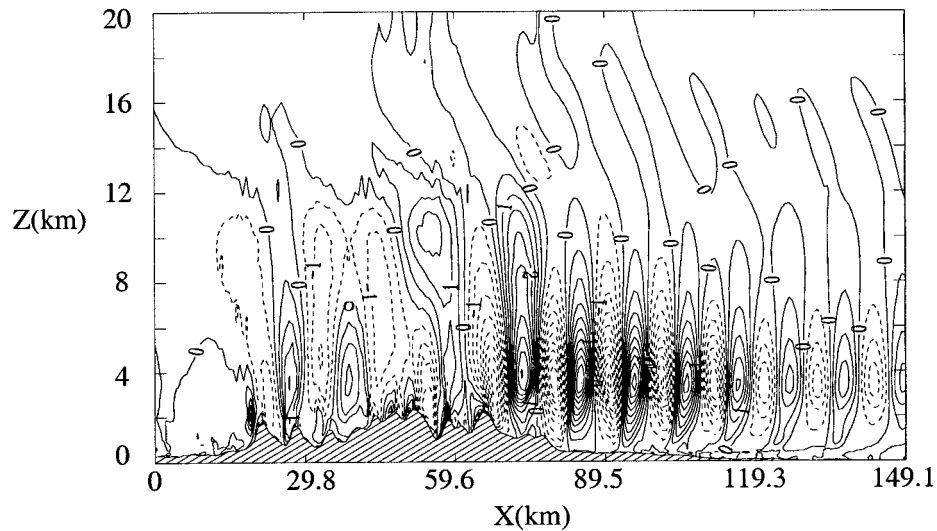
FIG. 14. Nonlinear simulation: vertical velocity field; contours every 0.5 m s^{-1}.

horizontal resolution is 700 m and the model has 60 levels with resolution varying from 50 m at the ground to 500 m at the top. An absorbing layer is set above 12 km and the topography is deduced from the aircraft measurements. The model includes the Bougeault and Lacarrere (1989) turbulent kinetic-energy boundary-layer parameterization scheme in its unidimensional version. Furthermore we already know that in the two-dimensional context the low-level flow blocking and the

FIG. 15. Vertical velocities at different altitude, superposition between airplane observations (thin solid) and the nonlinear simulation (thick solid).

associated reduction of the gravity wave forcing can not be simply accounted for. A way to deal with this without referring to the "cutoff mountain" approach, is to assume that the low-level flow blocking can be simulated in the two-dimensional context by decelerating the low-level flow in some way. In the meso-NH model, this can be done by specifying a large roughness length over the mountain: it will be set equal to 15 m in the experiment presented in section 4b, and sensitivity to this parameter is discussed in section 4c.

Before proceeding to more complete simulations, we verified that the two models converge; that is, that the meso-NH model, in a linear nondissipative configuration and with the incoming flow profile 2, reproduces the train of waves described in section 3. Compared to the conceptual case analyzed before, the sounding adopted is the Zaragosa sounding, that is, that located on the upstream foot, modified, as in Satomura and Bougeault (1994), to reconstitute missing data. This profile, as shown Fig. 7b, is rather near profile 3 everywhere between $Z = 0.5$ km and $Z = 10$ km.

b. Results

Figure 14 presents the vertical velocity field after 4 h of model integration and shows that the thickness of the trapped wave layer is about 8 km as in the linear simulation of section 3. As expected from the linear run with U profile 3, there is only one resonant mode with a wavelength $\lambda_x \approx 10.5$ km that is a little longer than in the observation. By scaling down the orography by a factor of 100, we verified that the horizontal wavelength is not much affected by changes in the mountain elevation.

Figure 15 presents a direct comparison with the aircraft measurements, after 4 h of integration. Observed and simulated vertical velocity are superimposed and
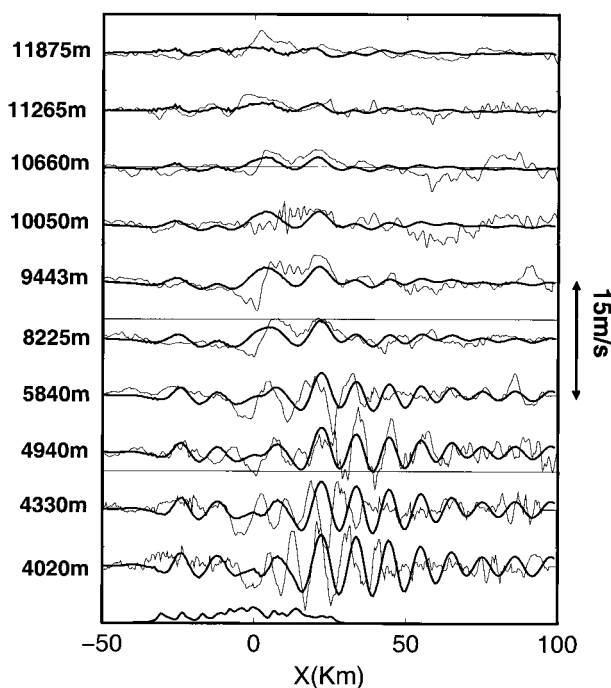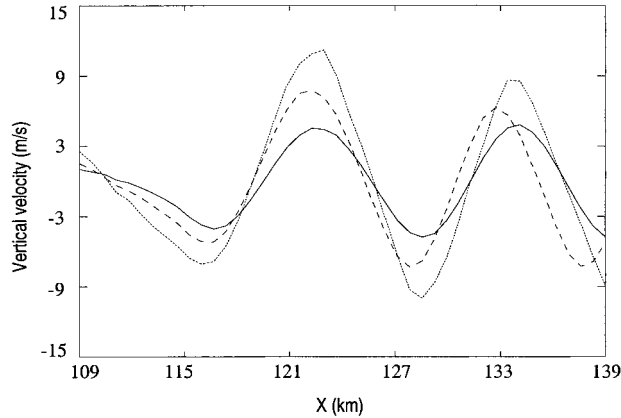
FIG. 16. Nonlinear simulation: vertical velocities at $Z = 4$ km with $Z_0 = 0.2$ m (dotted), $Z_0 = 2$ m (dashed), and $Z_0 = 15$ m (solid).

FIG. 17. Nonlinear simulation: time evolution of the 314-K isentrope at 1) 1130, 2) 1140, 3) 1145, 4) 1150, 5) 1210 UTC.

except for the first oscillation, the model agrees with the observation for the wave amplitude. The number of waves is nevertheless not correct in the simulation; they propagate up to the domain limit while in the observation they do not go far beyond 50 km downstream. Even if these differences can be due to 3D turbulence or 3D wave dispersion (Sharman and Wurtele 1983), section 3 has shown that a trapped wave that decays downstream so rapidly can be obtained in the early unsteady phase of a 2D simulation. The wave phase is also quite correct, but since both the observed and the simulated fields are unsteady this particular phase matching is more circumstantial. Indeed, after 4 h of integration, the wave field in the model is not stationary.

These results show that the addition of dissipative and nonlinear effects, insures that the wave amplitude is excellent above and slightly downstream the ridge. This matching was obtained for a roughness length value $Z_0 = 15$ m, which is known to be adapted, when one wishes to simulate mountain waves with realistic amplitudes (Georgelin et al. 2000). To a certain extent, in our simulation, this value compensates for the absence of blocking and for the fact that the nonlinear low-level flow goes around rather than over the ridge. Sensitivity tests using roughness lengths of 0.2 m and 2 m for the same configuration have been conducted in order to address the role of friction on the trapped wave amplitude. Figure 16 presents a comparison between the vertical velocity at $Z = 4.2$ km for the three different roughness lengths, it clearly shows that the wave amplitude decreases when the friction increases. The wave amplitude in the simulation with $Z_0 = 0.2$ m is close to the linear one, suggesting that, in a full nonlinear regime, the wave amplitude is controlled by frictional effects.

This sensitivity of the wave amplitude to friction is contrary to the small sensitivity found by Satomura and Bougeault (1994). This discrepancy can be explained by the fact that in the simulations presented by these authors, the turbulen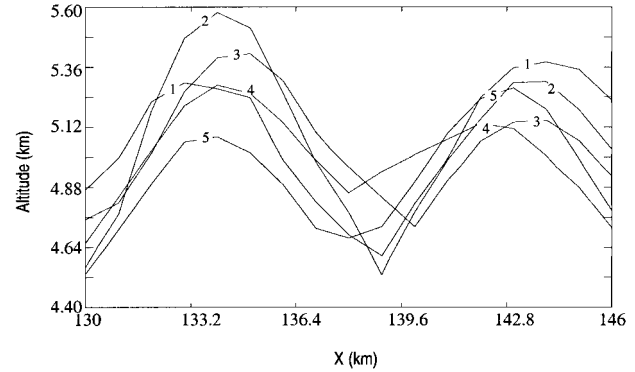t kinetic energy keeps close to the ground and does not interact much with the trapped waves whereas, in our simulations, turbulence forms a plume downwind of the mountain (not shown) and reaches 3.5 km of altitude, which corresponds (Fig. 14) to the altitude of the maxima of the vertical velocity. The strong value of the roughness length thus has an unexpected but realistic impact: a large zone of turbulence around 3–4 km of altitude is observed downwind of the Pyrénées during the IOP 3 (Bougeault et al. 1997).

c. Nonlinear instationarity

If the nonlinear run is extended up to 12 h, so that we can assume that the build-up phase is completed near aloft the ridge, the simulated trapped waves still appear strongly unsteady. This phenomenon has been studied by Nance and Durran (1998), who have shown that it is due to nonlinear wave interaction and that it is likely to produce lee wave fluctuation. Nance and Durran (1998) have also shown that the temporal variation of the wave crests form an elliptic hysteresis cycle. This effect is illustrated on Fig. 17, where the elevation of the 314-K isentrope is displayed five successive times. The summit of the crests describe an elliptical pattern in approximately 1 h.

d. Reynolds stress

An analysis of the Reynolds stress profiles and of the contribution of the trapped-resonant mode to that stress has been undertaken. They reveal that in all cases, the trapped waves contribute little to the stress. This is of course consistent with the linear simulation with U profile 3 in section 3. It shows that dissipative and nonlinear processes alone are not sufficient to explain the contribution of the resonant modes to the stress. Although this is based on a limited ensemble of simulation, it seems that within the limits provided by the observations, if the trapped modes do not transport momentum in the linear steady inviscid case, there are little chances that they will do so, under the combined action of dissipation and nonlinearity.

5. Discussion

The spectral analysis of the waves system observed by airplanes aloft the Pyrénées main transect during the PYREX IOP 3 reveals that two modes with wavelengths $\lambda_x \approx 8.5$ km and $\lambda_x \approx 15.5$ km are the most significant oscillatory signals that can be extracted from the data. As altitude increases, the amplitude of the shortest mode goes decreasing compared to that of the longest one. At long wavelengths the signal resembles a continuum of harmonics for which dynamical significance is not easy to test in the spectra of the vertical velocity only. Indeed, the null hypothesis chosen is that of a red noise, and the mountain-forcing spectra looks like a red-noise. Nevertheless, this continuum is nearer being significant in the cross-spectra between u' and w' at high altitude. This suggests that the u' and w' series are linked dynamically at long wavelengths, in the sense that they are more related one with one another than two independent random series. The cross spectral analysis also reveals that the two oscillations mentioned above contribute significantly to the momentum budget at low level. When cumulated over all wavelengths, their contribution to the stress is nearly half that stress value at low level. Their contribution drops sharply as altitude increases.

Following early studies interpreting the structure of observed waves using linear theory, we conduct linear two-dimensional simulations where the background flow specification are near that observed by the four soundings launched close to the PYREX transect—the 15 October 1999 around 0600 UTC. We also made extensive sensitivity tests, varying the background flow profiles within reasonable limits. These simulations reveal that (i) the onset of two resonant modes this day is quite natural and (ii) these resonant modes transport a significant fraction of momentum. Near $Z = 4$ km, the fraction of momentum transported by the resonant modes can be comparable to that transported by the free waves.

On the one hand, these findings complete those of Tannhauser and Attié (1995), who detected only one mode that day, and contradict them in that they concluded that this mode does not contribute to the momentum budget. Regarding the number of modes, that our findings and theirs contradict is not much surprising because these authors only had available the four lowest flights, while the long mode strongly manifests itself in only one among these. Regarding the role of the resonant modes in the momentum budget, that our findings and theirs contradict follows that the contribution of the shortest mode to the momentum budget is small around $Z = 5$ km. This altitude is near the turning height of the short-resonant mode; it is also below two of the four lowest level flights made this day. Our results partly recover those of Brown (1983) who has shown that the resonant modes can contribute to the Reynolds stress providing that they leak into the stratosphere. Again we complete his view since our analysis reveals that both trapped- and leaking-resonant modes can contribute to the stress at low level. The sensitivity tests we made further illustrate why the past numerical studies of trapped waves contradict with one another over the importance of the resonant modes to the momentum budget. By varying the background flow within reasonable limits, the number of resonant modes, their ability to leak into the stratosphere and the altitude up to which they contribute to the momentum budget vary considerably. Qualitatively, nevertheless, these sensitivity tests reveal important and robust behaviors. For instance, they show that the onset of more than one resonant mode this day is rather natural. They also show that all the resonant modes can participate to the momentum budget.

Compared to the observations, the linear simulations always overestimate (i) the distance between the wavelengths of the two resonant modes, (ii) the waves' amplitude, and (iii) the waves' downstream extent. They also do not explain (iv) how a leaking-resonant mode can have a stress that varies with altitude. In the limit of the experiments presented here, we reach the conclusion that the overestimate of the distance between the wavelengths of the resonant modes cannot be solved in the 2D context. The other three points can be solved if we consider unsteady simulations and use a cutoff mountain to crudely account for nonlinear effects. We then reach a linear simulation of 3 h, which matches the observations both with respect to the wave pattern observed (amplitude and downstream extent) and with respect to the contribution of the resonant modes to the stress below $Z = 5$ km and not above.

To address the role of nonlinear and dissipative effects alone, we have also conducted a limited number of experiments using the meso-NH model. Providing that low-level flow blocking is now simulated using a moderately strong value of the roughness length, these simulations show a good agreement with the observations as well. The quality of these simulations is in large part related to the fact that the boundary layer scheme in the model simulates a large zone of turbulence downstream and around 3–4-km altitude (incidently consistent with the observations). In addition, the nonlinear simulations give an illustration, in a realistic configuration, of the nonlinear wave nonstationarity described in Nance and Durran (1998). These nonlinear simulations are conducted for flow profiles where the resonant modes do not contribute much to the Reynolds stress in the steady inviscid case. Since the Reynolds stresses are small in all these simulations, they show that nonlinear dissipative processes alone cannot explain the observed contribution of the resonant modes to the Reynolds stress.

These results are relevant in the context of subgrid-scale orographic parameterization. They further legitimize the use of the cutoff mountain concept introduced in some subgrid-scale orography parameterization schemes (Lott 1999) to evaluate the part of the mountain

drag that is related to the waves only. To parameterize the contribution of the trapped waves to that drag is more difficult because it is strongly related to the resonant modes of the incident flow profile and to the orography spectrum. Nevertheless, it seems reasonable to associate each harmonic forced at the ground with a pseudo-momentum flux. Those that meet a turning height will carry that pseudo-momentum downstream. The variation with height of the Reynolds stress can be taken as the difference between the wave drag at the ground and that part of the drag associated to the waves that do not meet a turning height in the lower troposphere. If one assumes that the trapped waves are damped downstream, one can actually consider the Reynolds-stress divergence as a force acting on the large-scale flow. Our work further legitimizes that this force can be evaluated without knowing explicitly the processes that damp the trapped waves, as is currently done in the Gregory et al. (1998) and Lott (1999) parameterization schemes.

REFERENCES

Attié, J. L., A. Druilhet, P. Durand, and B. Benech, 1997: Two-dimensional structure of mountain wave observed by aircraft during the PYREX experiment. *Ann. Geophys.,* **15,** 823–839.

Bell, T. H., 1975: Lee waves in stratified flows with simple harmonic time dependence. *J. Fluid Mech.,* **67,** 705–722.

Benech, B., and Coauthors, 1994: Observation of lee waves above the Pyrenees (French Spanish PYREX experiment) and experimental assessment of the applicability of the linear theory. *Tech. Soaring,* **18,** 7–12.

Bessemoulin, P., P. Bougeault, A. Genoves, A. Jansa Clar, and D. Puech, 1993: Mountain pressure drag during PYREX. *Beitr. Phys. Atmos.,* **66,** 305–325.

Boer, G. J., N. A. McFarlane, R. Laprise, J. D. Henderson, and J. P. Blanchet, 1984: The Canadian climate center spectral atmospheric general circulation model. *Atmos.-Ocean,* **22,** 397–429.

Bougeault, P., 1994: Are 2D simulations a good approximation of orographic flows? An exemple from PYREX. *Proc. Sixth Conference on Mesoscale Processes,* Portland, OR, Amer. Meteor. Soc., 467–470.

——, and P. Lacarrère, 1989: Parameterization of orography-induced turbulence in a mesobeta-scale model. *Mon. Wea. Rev.,* **117,** 1872–1890.

——, A. Jansa Clar, B. Benech, B. Carissimo, J. Pelon, and E. Richard, 1990: Momentum budget over the Pyrénées: The PYREX experiment. *Bull. Amer. Meteor. Soc.,* **71,** 806–818.

——, and Coauthors, 1993: The atmospheric momentum budget over a major atmospheric mountain range: First results of the PYREX program. *Ann. Geophys.,* **11,** 395–418.

——, A. Jansa Clar, B. Benech, B. Carissimo, J. Pelon, and E. Richard, 1997: PYREX: A summary of findings. *Bull. Amer. Meteor. Soc.,* **78,** 637–650.

Bretherton F. P., 1969: Momentum transport by gravity waves. *Quart. J. Roy. Meteor. Soc.,* **95,** 213–243.

Broad, A. S., 1996: High-resolution numerical-model integrations to validate gravity-wave-drag parameterization schemes: A case-study. *Quart. J. Roy. Meteor. Soc.,* **122,** 1625–1653.

Brown, P. A., 1983: Aircraft measurements of mountain waves and their associated momentum flux over the British Isles. *Quart. J. Roy. Meteor. Soc.,* **109,** 849–865.

Clark, T. L., and R. Gall, 1982: Three-dimensional numerical model simulations of airflow over mountainous terrain: A comparison with observations. *Mon. Wea. Rev.,* **110,** 766–791.

Durran, D. R., 1995: Do breaking mountain waves decelerate the local mean flow? *J. Atmos. Sci.,* **52,** 4010–4032.

——, 1986: Another look at downslope winds. Part 1: The development of analogs to supercritical flow in an infinitely deep, continuously stratified fluid. *J. Atmos. Sci.,* **43,** 2527–2543.

Eliassen, A., and E. Palm, 1961: On the transfer of energy in stationary mountain waves. *Geophys. Norv.,* **22,** 1–23.

Elkhalfi, A., and B. Carissimo, 1993: Numerical simulations of a mountain wave observed during the Pyrénées Experiment: Hydrostatic/nonhydrostatic comparison and time evolution. *Contrib. Atmos. Phys.,* **66,** 183–200.

Georgelin, M., E. Richard, M. Petitdidier, and A. Druilhet, 1994: Impact of subgrid-scale orography parameterization on the simulation of orographic flows. *Mon. Wea. Rev.,* **122,** 1509–1522.

——, and Coauthors, 2000: The second COMPARE exercise: a model intercomparison using a case of a typical mesoscale orographic flow, the PYREX IOP 3. *Quart. J. Roy. Meteor. Soc.,* **126,** 991–1029.

Gregory, D., G. J. Shutts, and J. R. Mitchell, 1998: A new gravity-wave-drag scheme incorporating anisotropic orography and low-level wave breaking: Impact upon the climate of the UK meteorological office unified model. *Quart. J. Roy. Meteor. Soc.,* **124,** 463–493.

Hamming, R. W., 1983: *Digital Filters.* Prentice-Hall, 296 pp.

Hoinka, K. P., and T. L. Clark, 1991: Pressure drag and momentum fluxes due to the Alps. Part I: Comparison between numerical simulations and observations. *Quart. J. Roy. Meteor. Soc.,* **117,** 495–525.

Keller, T. L., 1994: Implications of the hydrostatic assumption on atmospheric gravity waves. *J. Atmos. Sci.,* **51,** 1915–1929.

Lafore, J. P., and Coauthors, 1998: The Meso-NH Atmospheric Simulation System. Part I: Adiabatic formulation and control simulations. *Ann. Geophys.,* **16,** 90–109.

Laprise, R., and W. R. Peltier, 1989: The structure and energetics of transient eddies in a numerical simulation of breaking mountain waves. *J. Atmos. Sci.,* **46,** 565–585.

Lipps, F. B., and R. S. Hemler, 1982: A scale analysis of deep moist convection and some related numerical calculations. *J. Atmos. Sci.,* **39,** 2192–2210.

Long, R. R., 1953: Some aspects of the flow of stratified fluids. 1. A theoretical investigation. *Tellus,* **5,** 42–57.

Lott, F., 1998: Linear mountain drag and averaged pseudo-momentum flux profiles in the presence of trapped lee waves, *Tellus,* **50A,** 12–25.

——, 1999: Alleviation of stationary biases in a GCM through a mountain drag parameterization scheme and a simple representation of mountain lift forces. *Mon. Wea. Rev.,* **127,** 788–801.

——, and H. Teitelbaum, 1993: Topographic waves generated by a transient wind. *J. Atmos. Sci.,* **50,** 2607–2624.

——, and M. Miller, 1997: A new subgrid scale orographic drag parameterization; its testing in the ECMWF model. *Quart. J. Roy. Meteor. Soc.,* **123,** 101–127.

McIntyre, M., 1980: An introduction to the generalized Lagrangian-mean description of wave, mean-flow interaction. *Pure Appl. Geophys.,* **118,** 152–176.

Miller, M. J., T. N. Palmer, and R. Swinbank, 1989: Parameterization and influence of subgridscale orography in general circulation and numerical weather prediction models. *Meteor. Atmos. Phys.,* **40,** 84–109.

Miranda, P. M. A., and I. A. James, 1992: Non-linear three dimensional effects on gravity-wave drag: Splitting flow and breaking waves. *Quart. J. Roy. Meteor. Soc.,* **118,** 1057–1081.

Nance, L., and D. R. Durran., 1998: A modeling study of nonstationary trapped mountain lee waves, Part II: Nonlinearity. *J. Atmos. Sci.,* **55,** 1429–1445.

Palmer, T. N., G. J. Shutts, and R. Swinbank, 1986: Alleviation of systematic westerly bias in general circulation and numerical weather prediction models through an orographic gravity wave drag parameterization. *Quart. J. Roy. Meteor. Soc.,* **112,** 2056–2066.

Phillips, D. S., 1984: Analytical surface pressure and drag for linear hydrostatic flow on three dimensional elliptical mountains. *J. Atmos. Sci.,* **41,** 1073–1084.

Queney, P., 1947: *Theory of Perturbations in Stratified Currents with Application to Airflow over Mountains.* The University of Chicago Press, 81 pp.

Satomura, T., 1996: Supplement to numerical simulation of lee-wave events over the Pyrenees. *J. Meteor. Soc. Japan,* **74,** 147–153.

——, and P. Bougeault, 1994: Numerical simulation of lee wave events over the Pyrenees. *J. Meteor. Soc. Japan,* **72,** 173–195.

Scavuzzo, C. M., M. A. Lamfri, H. Teitelbaum, and F. Lott, 1998: A study of the low frequency inertio-gravity waves observed during PYREX. *J. Geophys. Res.* **103** (D2), 1747–1758.

Schär, C., and R. B. Smith, 1993: Shallow water flow past isolated topography. Part 1: Vorticity production and wake formation. *J. Atmos. Sci.,* **50,** 1373–1400.

——, and D. R. Durran, 1997: Vortex formation and vortex shedding in continuously stratified flows past isolated topography. *J. Atmos. Sci.,* **54,** 534–554.

Scinocca, J. F., and T. G. Shepherd, 1992: Nonlinear wave-activity conservation laws and Hamiltonian structure for the two-dimensional anelastic equations. *J. Atmos. Sci.,* **49,** 5–27.

Scorer, R., 1949: Theory of waves in the lee of mountains. *Quart. J. Roy. Meteor. Soc.,* **75,** 41–56.

Sharman, R. D., and M. G. Wurtele, 1983: Ship waves and lee waves. *J. Atmos. Sci.,* **40,** 396–427.

Shepherd, T. G., 1990: Symmetries, conservation laws and hamiltonian structure in geophysical fluid dynamics. *Advances in Geophysics,* Vol. 32, Academic Press, 287–338.

Smith, R. B., 1980: Linear theory of stratified hydrostatic flow past an isolated mountain. *J. Atmos. Sci.,* **32,** 348–364.

——, 1985: On severe downslope winds. *J. Atmos. Sci.,* **42,** 2597–2603.

Smolarkiewicz, P. K., and R. Rotunno, 1989: Low Froude number flow past three-dimensional obstacles. Part 1: Baroclinically generated lee vortices. *J. Atmos. Sci.,* **46,** 1154–1164.

Tannhauser, D. S., and J. L. Attié, 1995: Linear analysis of the wave field during a lee wave event of the PYREX campaign. *Meteor. Z.,* **4,** 203–208.

Vergeiner, I., 1971: An operational linear lee wave model for arbitrary basic flow and two-dimensional topography. *Quart. J. Roy. Meteor. Soc.,* **97,** 30–60.

Wurtele, M. G., and R. D. Sharman, and T. L. Keller, 1987: Analysis and simulations of a troposphere–stratosphere gravity wave model. Part I. *J. Atmos. Sci.,* **44,** 3269–3281.